

Guided plate wave scattering at vertical stiffeners and its effect on source location

R. S. Reusser, D. E. Chimenti, R. A. Roberts, S. D. Holland
Center for Nondestructive Evaluation
and Aerospace Engineering Department
Iowa State University
Ames IA 50011 USA

October 14, 2011

Abstract

This paper examines the influence of guided wave transmission characteristics of plate stiffeners on the performance of acoustic noise source location technology. The motivation for this work is the detection of turbulence-generated noise by a contact-coupled acoustic array, to perform source location and find the air leak (in a manned spacecraft) responsible for the noise. Transmission characteristics of individual integral stiffeners are measured across a frequency range of 50 to 400 kHz for both high and low aspect-ratio rectangular stiffeners, and comparisons are made to model predictions which display generally good agreement. It is demonstrated that operating in frequency ranges of high plate wave stiffener transmission significantly improves the reliability of noise source location in the plate. A protocol is presented to enable the selection of an optimal frequency range for leak location.

1 INTRODUCTION

In this paper we investigate the influence of rectangular geometric obstructions, such as integral stiffeners typical in aerospace structures, on guided plate wave propagation. The motivation for the work is the development of a method to exploit noise generated by turbulence that occurs when air leaks through a small orifice into vacuum at a pressure differential of about one atmosphere. The situation is intended to model a small air leak

in a manned spacecraft, such as the International Space Station (ISS), where scientific equipment and life support systems preclude rapid location of a meteorite or debris-caused air leak in the spacecraft pressure vessel wall because of its inaccessibility [?, ?]. Although turbulence-generated airborne noise is the conventional method of locating leaks in terrestrial pressurized systems, because the air leaks from inside the occupied spacecraft into the vacuum of space, there is almost no airborne noise generated inside the spacecraft. The method we have reported [?] relies instead on ultrasonic noise (20-400 kHz) generated by the leak in the skin of the spacecraft structure, through aerodynamic coupling of the escaping air to the plate-like pressure vessel wall. Because the diameter of the spacecraft is much larger than the longest ultrasonic wavelength, the vessel wall can be accurately modeled as a flat plate [?]. An acoustic array provides directional information on the arriving noise signals. Temporal correlations extract the statistics of the noise signal phase arriving at one array element compared to signals from all the other elements of the array. Because the signals are random and continuous, the signal acquisition and processing can proceed sequentially, significantly reducing the expense of the electronics. Processing algorithms based on two-dimensional spatial Fourier analysis similar to that of Alleyne and Cawley [?] yield an estimate of the direction to the noise signal source. With two or more arrays, triangulation locates the leak.

Our own prior work [?, ?] has shown that boundaries or geometric obstructions may limit performance of the leak location procedure by causing acoustic echoes or reverberations. That work focused on the development of a detector capable of sensing the dispersive Lamb modes coupled into a plate at the source of a leak. Successful leak location has been demonstrated on simulated spacecraft structure using an 64-element diced PZT (lead zirconate titanate) piezoelectric array detector [?]. In an environment where prompt and accurate leak location is critical, the procedure must be accurate and robust, so the current work focuses on a study of guided wave propagation in spacecraft structure and the development of a method to select the optimal detection center frequency and bandwidth.

One of the main factors influencing leak location reliability is the geometry of the

spacecraft structure itself. To add additional rigidity and strength with minimal weight, spacecraft structures typically include integral stiffeners machined into the structure. These stiffeners scatter the leak-generated noise signal, and based on Boundary Element Method (BEM) calculations [?], it has been shown that the stiffening ribs act like a frequency-dependent filter, producing frequency bands with high transmission across stiffeners, and frequency bands with low transmission. Despite the complication represented by the stiffeners, the location system described above has been shown to perform well in integrally stiffened plates [?], provided the frequency range for analysis is carefully chosen to avoid regions where guided wave transmission across stiffeners is low.

In this paper we report measurements of guided wave transmission across two types of stiffeners and compare experimental data to the results of BEM calculations. Optical laser vibrometer detection — similar to that employed by Morvan et. al. [?] to measure guided wave reflection from the free edge of a plate — has been chosen to suppress the sometimes inconsistent influence of acoustical coupling between the contact array sensor and the aluminum plate. Acoustical coupling variations can make the received signal amplitude difficult to reproduce after detachment and re-attachment of the array sensor.

In addition, we demonstrate a method to choose an optimal frequency range in which to perform robust leak location measurements. We find that guided wave transmission measurements using a piezoelectric point source and an optical virtual array receiver agree well with the BEM calculations over a frequency range of 50 to 400 kHz for two types of stiffener geometry when the incident guided wavevector is at, or near, normal incidence on the stiffener. As a by-product of our investigation we have developed a frequency selection protocol to assist with the application of the method to leaks in many kinds of spacecraft with arbitrary rectangular obstructions. We find that it is best to include the entire frequency range in the active analysis, because when integrated over the entire detection spectrum, the frequency range that produces accurate results dominates the ranges that do not. In what follows, we will present the scattering measurements and theoretical summary first, followed by our proposed detection protocol.

2 EXPERIMENTAL TECHNIQUE

2.1 Sample geometry

Two aluminum samples have been studied in these experiments. The first has a thickness of 3.175 mm (1/8 inch) with stiffeners having a square cross section of 4.76×4.76 mm machined directly into the plate, so there is no material boundary between the plate and the stiffener. Sound-absorbing putty is layered around the active experimental area so that reflections are almost completely suppressed, even at the lowest frequency of 50 kHz, to isolate the response of a single plate stiffener. The second plate is a sample obtained from a major aerospace company involved in the construction of ISS components. The sample dimensions are a thickness of 4.76 mm with stiffeners 2.54 mm wide and 22 mm in height. The absorbant layer of uncured butyl rubber putty assures reliable measurements that can be confidently compared to the results of an idealized calculation. A representation of the experimental geometry is shown in the inset of Fig. 1. The incident, reflected, and transmitted waves are shown for the short, or low aspect-ratio, stiffeners.

2.2 Experimental Technique

A Polytec OFV-5000/OFV-505 Laser Vibrometer measures the out-of-plane particle velocity on the plate surface at both the incident and transmission sides of the stiffener. The vibrometer is mounted on a two-axis motion control stage which translates the entire laser for horizontal control and deflects the beam with a mirror for vertical control. At the frequencies involved, the sensitivity of the laser vibrometer is very poor compared piezoelectric sensors. A point contact horn on the source transducer best approximates a point source, but is inefficient. Because of both of these conditions, transducer 10^4 averaged impulse responses at a simulated leak source, acquired at a rate of 100 Hz, provide the desired signal-to-noise ratio. To achieve the best results, the full usable spans of the plates are scanned with 1 mm spacing.

A 9.5-mm diameter contact transducer coupled to a non-resonant ultrasonic horn

with a contact area of roughly 1mm^2 induces guided waves in the plates. A Panametrics Pulser-Receiver excites the transducer impulsively, and the transducer is fixed to the specimen with couplant and light pressure for the duration of the test to prevent non-repeatability. Because of asymmetric single-side excitation, most of the energy resides in the A_0 , or lowest order antisymmetric, Lamb mode.

Figure 1 shows a photograph of the low aspect-ratio specimen with absorbing butyl rubber applied at the perimeter of the experimental area. The cross denotes the location

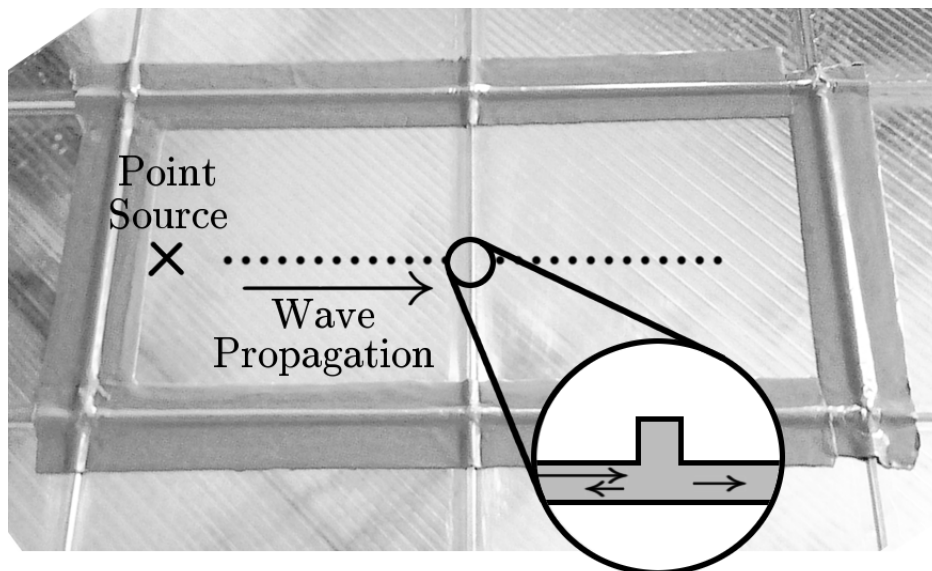


Figure 1: Photo of 6×6 -foot sample showing experimental area isolated by butyl rubber (seen as a low-reflection band on the perimeter). Source is marked with a cross, and two sets of dots show the locations of laser vibrometer linear virtual-array measurements of incident and scattered guided wave fields. Inset shows stiffener cross-section with arrows representing waves incident upon as well as transmitted and reflected by stiffener.

of the contact source transducer, and two independent 1-dimensional coordinate scans with the laser vibrometer (indicated by the lines of circles) measure the incident and transmitted waves. Because the signal is repeatable only a single measurement need be made at a time. The butyl rubber inhibits undesirable reflections, and data is captured until all ringing and wave propagation have decayed to below the noise threshold. Different arrangements of the point source and array receivers were considered, but only this arrangement has produced acceptable results since incident and reflected waves are

easily filtered in frequency-wavenumber space.

2.3 Analysis

Integral stiffeners scatter guided Lamb modes in a complex fashion, as will be explained later. The stiffeners reflect and transmit the signal depending on frequency, aspect ratio, guided wave mode, and incident angle, acting as frequency-dependent filters of the excitation signal. Certain frequency bands have high transmission and other frequency bands have high reflection [?]. Transmission across the stiffener seems to be related to resonances which, in the case of non-normal incidence map to feature-guided waves that propagate along the stiffener [?, ?]. In our case, we look at normal incidence with the expectation that our results can be extrapolated based on this theory.

A single incident mode may be mode-converted into multiple scattered modes. The overall behavior is represented with an energy transmission coefficient, defined at frequency ω by

$$T(\omega) = \frac{\sum_n E_n^{\text{tr}}(\omega)}{\sum_n E_n^{\text{inc}}(\omega)}, \quad (1)$$

where E_n^{tr} and E_n^{inc} are the transmitted and incident energies of the n^{th} guided wave modes, respectively. Because only the A_0 and S_0 modes exist at low frequency, and because the A_0 mode dominates over the symmetric mode under the asymmetric excitation used in our experiments, only the A_0 mode need be considered. With that simplification, the transmission coefficient is

$$T(\omega) \approx \frac{E_{A_0}^{\text{tr}}(\omega)}{E_{A_0}^{\text{inc}}(\omega)}. \quad (2)$$

Neglecting phase and assuming a mode-dependent constant of proportionality \mathcal{C}_{A_0} between the square of signal amplitude A and energy E for this mode, the expression can further be simplified to

$$T(\omega) \approx \frac{\mathcal{C}_{A_0} |A_{A_0}^{\text{tr}}(\omega)|^2}{\mathcal{C}_{A_0} |A_{A_0}^{\text{inc}}(\omega)|^2} = \frac{|A_{A_0}^{\text{tr}}(\omega)|^2}{|A_{A_0}^{\text{inc}}(\omega)|^2}, \quad (3)$$

where the amplitudes are measured with the laser vibrometer. To correct for radial falloff

of the waves as they spread in two dimensions, the signal measurements are normalized by $1/\sqrt{r}$, where r is the distance from the noise source to the measurement location.

Because the measured guided wave amplitude will be a superposition of incident and reflected waves as well as waves reflected from the boundaries, amplitudes are sampled along a line containing the source and perpendicular to the stiffener, as depicted in Fig. 1. A spatio-temporal Fourier transform of the measured signal, as described by Sachse and Pao [?], permits separation of the modes and guided wave propagation directions in frequency-wavenumber space.

2.4 Model Comparison

Experimental measurement of the stiffener transmission frequency dependence is corroborated through comparison to model predictions. Computational models of stiffener transmission were previously developed and reported in support of this work [?, ?]. A brief verbal summary of the model formulation will be presented here. More detailed mathematical descriptions of model formulation and implementation can be found in the cited references.

The modeling approach uses a boundary integral equation formulation to determine wave motions on the surface of the stiffening rib. The model used to obtain the predictions presented in this work segments the problem into a body which joins multiple semi-infinite plates. The geometry of the joining body is restricted to one of extrusion, i.e., its cross-sectional profile is invariant in the direction of the semi-infinite plate edges that attach to it. The geometry of the joining body is otherwise arbitrary. The guided wave field which impinges on the joining body through one of the attached plates can likewise be arbitrary in geometry. However, the comparison presented in this paper restricts consideration to the special case of plate wave incidence having a linear phase front oriented parallel to the semi-infinite plate edge, and uniform displacement amplitude in the direction of the phase front. Consequently, the problem formulation is inherently two-dimensional in nature.

The joining body is prescribed to be a short section of plate to which is attached a stiffening rib, as depicted in Figure 1. Application of reciprocity relations to the surface of the joining body for two possible wave fields, one of them being that arising from the incident plate wave, and the other being the Green function for a point load acting in an infinite 2D space of like material (a line load if perceived in 3D), leads to an integral equation relating the two fields over the surface of the joining body [?]. This integral equation is solved using the Boundary Element Method (BEM), which transforms the integral equation into a matrix equation for determination of the surface wave field by approximating the surface field as piece-wise quadratic polynomials (the boundary elements). On traction free surfaces of the joining body, the computation solves for surface displacements. On the surfaces to which the semi-infinite plates attach, the computation solves for surface tractions.

A key feature of the model is the approach used to related surface displacements to surface tractions on the surfaces to which the semi-infinite plates attach (plate attachment surfaces). For this purpose, impedance relations are pre-computed which tabulate the surface displacements over a plate edge resulting from an applied traction corresponding to each individual basis function used to represent the surface tractions on the plate attachment surface. The computational model for evaluating the impedance relation is likewise formulated as a boundary integral equation. In this case reciprocity relations are applied to the semi-infinite plate, relating the sought wave field to the Green function for a point load acting in an infinite plate. Use of the infinite plate Green function reduces the domain of computation to the edge of the semi-infinite plate. Application of the Boundary Element Method to this domain yields a matrix equation which is inverted to obtain the desired impedance relation.

After determining the surface wave field on the joining body for a specified incident guided wave, guided wave transmission and reflection coefficients are evaluated by a third application of wave field reciprocity. In this case, reciprocity is expressed between the guided wave fields propagating the semi-infinite plates resulting from transmission or reflection at the joining body, and the Green function for a point load acting in an infinite

plate, where the point load is acting at a large distance from the semi-infinite plate edge (far-field evaluation). As with the calculation of the impedance relation, use of the infinite plate Green function reduces the domain of integration to the plate edge, over which the wave field is known through the BEM solution of the joining body problem. In the case of far-field evaluation, the Green function takes the form of a sum of propagating plate modes, each term of which when used in the reciprocity relation yields the corresponding transmission/reflection coefficient for the mode of that type, such as represented in Eq. (3).

In applying the computational model to the low aspect ratio stiffener (4.76×4.76 mm), 5 boundary segments were prescribed on each face of the stiffener, and on each plate attachment surface, yielding a total of 30 segments. On each segment, a second order polynomial is used to represent the sought wave field, requiring 3 weighting coefficients. Solving for two components of either displacement or surface traction thereby required inversion of a 180×180 boundary element matrix. The width and height of the high aspect ratio stiffener (2.55×22 mm) was subdivided into 2 and 15 segments, respectively, with 5 segments prescribed over the plate attachment surfaces, leading to inversion of a 264×264 boundary element matrix.

3 RESULTS AND DISCUSSION

3.1 Guided wave transmission across stiffeners

Figure 2 shows a portion of the measured $x - t$ diagram for scattering from the tall stiffener. The normal component of the velocity magnitude is plotted in a logarithmic gray-scale (higher amplitude, darker value) from $t = 0$ to $t = 250\mu\text{s}$ and in coordinate from the source at $x = 0$ to the stiffener at $x = 325$ mm and beyond out to 550 mm from the source, both segments acquired with 1 mm spacing. Visible in the data are the incident S_0 and A_0 modes, separated by a factor of approximately 10 in amplitude. The faster S_0 mode meets the stiffener earlier at $t \approx 65\mu\text{s}$. In transmission past $x = 325$ mm there is still energy in the S_0 mode, although mode conversion to the flexural A_0 is

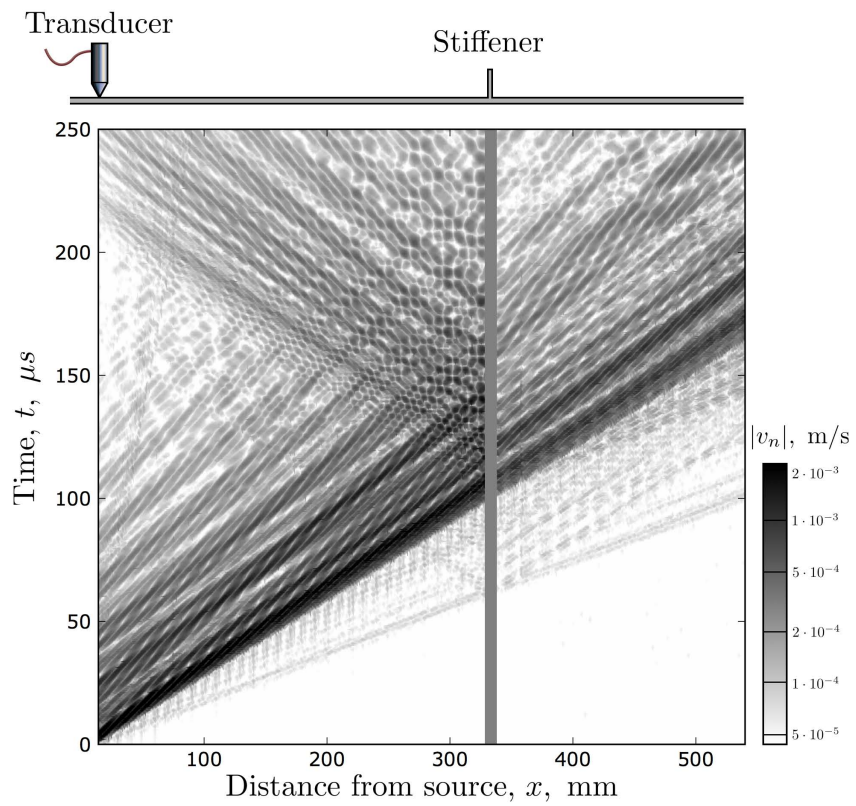


Figure 2: Measured normal component of particle velocity magnitude displayed as a gray-scale plot in coordinate x and time t for the tall stiffener test section. The wave amplitude is represented by the surface particle velocity v_n

seen both in the reflected and transmitted waves. (The angle of the wave departing the stiffener reveals its speed.) When the stronger, but slower, A_0 waves meet the stiffener at $t = 100\mu\text{s}$, there is significant reflection and transmission of energy without mode conversion. A very close examination shows that a small amount of $A_0 \rightarrow S_0$ mode conversion does occur in the transmitted waves. Interestingly, on the left side of the figure the vibrometer detects a very faint, and very slow, acoustic wave which appears as a faint line from the source to about 80 mm at $t = 250\mu\text{s}$. The wave speed matches the 340 m/s speed an acoustic wave travels in air.

The measured incident wave spectrum, measured along the radial line between source and stiffener is shown in Fig. 3. Data from a series of points along almost the entire distance from source to stiffener were compensated for geometric attenuation, Kaiser windowed, and Fourier transformed in space and time to give the grayscale amplitude as a function of wavenumber and temporal frequency [?]. The data fall onto discrete

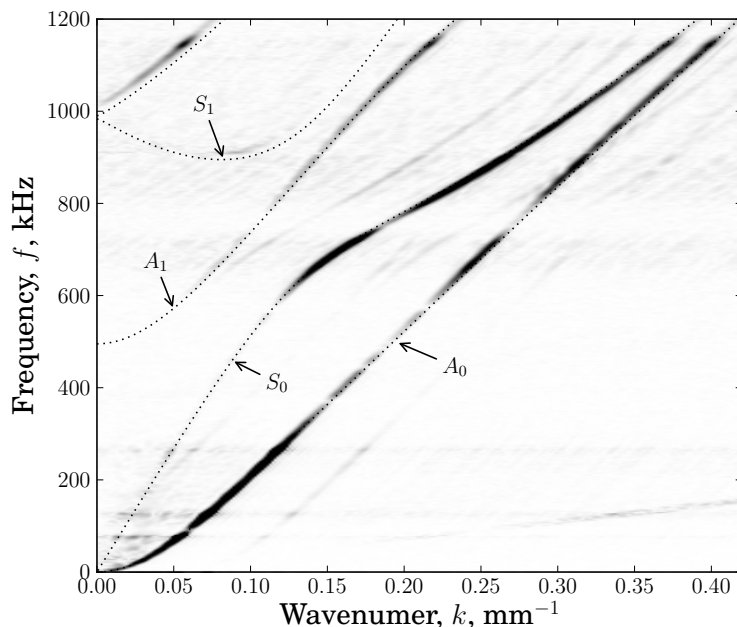


Figure 3: Measured dispersion curves for incident guided plate waves in the high aspect-ratio test section. Calculate Lamb wave dispersion curves (dotted lines) are superimposed.

mode curves. The curves coincide with normal modes of the plate, *i.e.*, Lamb waves.

The measured signal amplitude appears to be discontinuous because the excitation is related to the degree of out-of-plane motion at each point in the dispersion curve. Higher normal wave motion leads to a larger detected amplitude, such as between 100 and 300 kHz and 0.05 to 0.15 mm^{-1} in the wavenumber. This branch is the A_0 , or lowest order flexural, mode. It is strongly excited by the contact transducer on one side of the plate only because of the asymmetric aspect of the excitation. Between 600 and 900 kHz the lowest order symmetric mode S_0 is also rather strongly excited, but very little below 500 kHz.

The experimental energy transmission coefficients for the low aspect-ratio stiffener are calculated via Eq. (3) by sampling amplitudes along the A_0 mode in Figure 3 for incident and transmitted waves. The measured result and the result of the BEM computation are shown in Fig. ?? (a) and (b), respectively.

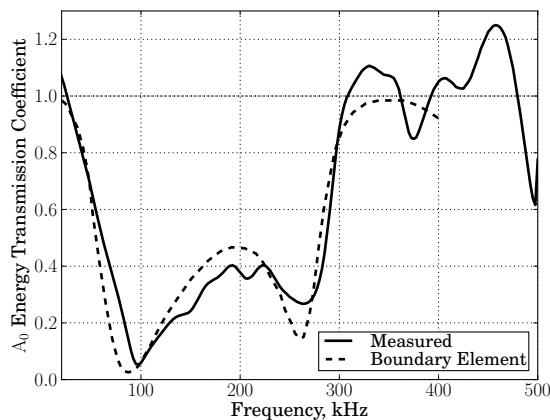


Figure 4: (a) Experimental and (b) theoretical energy transmission coefficients across the low aspect ratio stiffener, with the incident guided wave at normal incidence to the stiffener. The theoretical curve is the result of the boundary element method calculation.

The general shape of the two curves is similar. Both start at a transmission coefficient of 1.0 in the low frequency regime and have relative minima at approximately 100 and 260 kHz. The transmission coefficient increases to approximately 1.0 above 300 kHz. The experimental analysis neglects mode conversion of incident S_0 energy into transmitted A_0 . The small percentage of transmitted A_0 energy originating from S_0 allows the

transmission coefficient to appear to slightly exceed 1.0.

Fig. ?? (a) and (b) show the BEM and measured transmission coefficients of a high aspect ratio stiffener, respectively. The BEM and measured coefficients share a periodic structure with with a period of roughly 70 kHz and minima around 120, 190 and 250 kHz. This confirms the passband/stopband nature of the stiffeners when interacting with guided waves. The observed discrepancy in Fig. ?? owes in part to an extreme sensitivity (valided by simulation) of the exact stopband frequencies to stiffener geometry and material properties in this high aspect-ratio configuration. The model assumes a rectangular stiffener, with dimensions estimated by caliper measurements. The actual stiffener deviates somewhat from the assumed rectangular shape, including features such as filleted corners at the stiffener-plate junction. As for the low aspect-ratio stiffener, assumptions regarding the dominant A_0 mode again result in transmission coefficients slightly greater than the theoretical values.

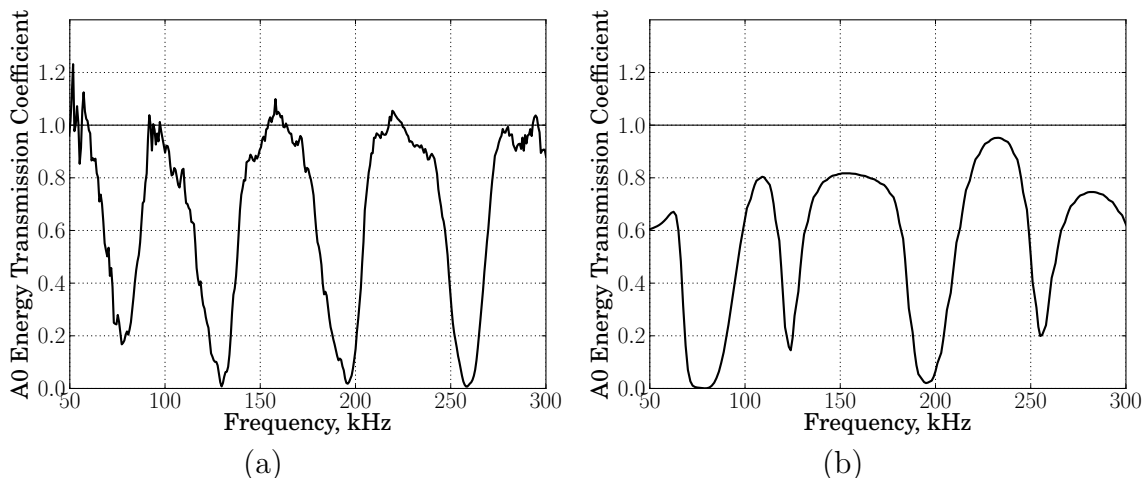


Figure 5: (a) Experimental and (b) theoretical energy transmission coefficients across the tall aspect-ratio stiffener, with the incident guided wave at normal incidence to the stiffener. The theoretical curve is the result of the boundary element method calculation.

The narrow stop bands observed in Fig. ?? for the high aspect ratio stiffener are the signature of a resonance. Transmission is blocked when the phase of the incident wave and the phase of a reflection in the stiffener come into alignment. For the low aspect ratio stiffener, we hypothesize that such a resonance is less well defined, hence

the broader relative bandwidth of the stop-band. If true, this would be very important for all structural health monitoring applications because wide stop bands would tend to block 50% of the ultrasonic signal bandwidth when crossing a stiffener.

3.2 Detection frequency and range selection

The device developed to realize the ideas presented in the introduction is a 64-element piezoelectric array [?] coupled to the plate using various coupling gels to achieve a level of consistency in the readings. Even with great care, however, some acoustical coupling variation is unavoidable. To bypass the experimental uncertainty represented by such variations, we have chosen in these experiments to conduct the tests using the same laser vibrometer optical probe described above, in place of the piezoelectric array. While the measurement with the laser vibrometer is not identical to the one with the PZT array, it does have the benefit of eliminating acoustical coupling variations, thus establishing a baseline for ideal PZT array performance. To compensate for the decreased sensitivity of the laser vibrometer relative to the PZT array, we use a piezoelectric impulse “point source” that mimics the leak, instead of the 2–4 mm hole backed by a high-volume vacuum pump, that was used to verify the performance of the PZT array [?]. This substitution is justified because the leak location concept has been fully proven in prior work.

The source transducer is fitted with a short concentrator horn attached to the transducer with salol and is excited with a Panametrics pulser/receiver in a manner identical to the stiffener transmission tests. The laser vibrometer virtual array consists of a 12×12 scanned point array on a 27.5×27.5 mm area with 2.5 mm spacing between the optical beam points. The out-of-plane motion is captured with the laser vibrometer using 200 triggers per point, averaged. Fewer averages are needed here than the 10^4 needed for the stiffener transmission measurement because the very high signal-to-noise ratio is not required and because the measured response can be integrated over frequency. Because of the critical aiming requirements, the optical array location is not moved. Instead, the piezoelectric source transducer is attached to the plate with mild pressure and a very thin layer of butyl rubber for acoustic coupling and is moved to simulate different leak

locations relative to the stiffener.

The replacement of the air leak with a known pulsed source changes slightly the signal processing from the leak case because the excitation is now deterministic, and cross-correlations are unnecessary. The interpretation, however, is unchanged. To summarize the method briefly, the signal generated by the source and arriving at the j th element of the detector array can be expressed, for distance $|\mathbf{x}_j| \gg 1/k_n(\omega)$, as

$$V(\mathbf{x}_j, \omega) = N(\omega) |\mathbf{x}_j|^{-1/2} \sum_n A_n(\omega) \exp(i k_n(\omega) |\mathbf{x}_j|), \quad (4)$$

where V represents the voltage at the j th vector position \mathbf{x}_j and frequency ω . The term N represents the complex amplitude and phase of the noise source, and the propagating waves are summed over all guided wave modes n with amplitude coefficient A_n . We can represent the j th array element vector position \mathbf{x}_j as the sum of the array reference position \mathbf{x}_0 and a relative element position \mathbf{s}_j ,

$$\mathbf{x}_j = \mathbf{x}_0 + \mathbf{s}_j. \quad (5)$$

The distance to a specific element can be written using the far-field approximation as

$$|\mathbf{x}_j| = |\mathbf{x}_0| + \mathbf{d} \cdot \mathbf{s}_j, \quad (6)$$

where \mathbf{d} is a unit vector pointing from the leak coordinates to the fixed reference position. Then, substitution into Eq. (??) yields

$$V(\mathbf{s}_j, \omega) = N(\omega) |\mathbf{x}_0|^{-1/2} \sum_n A_n(\omega) \exp[i k_n(\omega) (|\mathbf{x}_0| + \mathbf{d} \cdot \mathbf{s}_j)]. \quad (7)$$

The detector array (PZT or laser vibrometer) is not infinitely large, so its finite spatial extent means that a spatial window function $W(\mathbf{x})$ is applied to the acquired data. The two-dimensional Fourier transform of Eq. (??) in transform variables k and ω gives

$$\text{FT} \{W(\mathbf{x})V(\mathbf{x}, t)\} = \sum_n B_n \widehat{W}(\mathbf{k} - k_n \mathbf{d}), \quad (8)$$

where the amplitude coefficients have been grouped into B_n . Representing the data in a two-dimensional wavenumber map, the energy in all modes n and at frequency ω lies along

a line emanating from the origin and in the dominant direction of wave propagation \mathbf{d} . This direction can then be discerned by inspection of the map. Summing over a particular frequency range $\Delta\omega$ enhances the detectability of the leak. This operation results in a much improved detection accuracy and a more robust leak location method. Suppressing the parametric dependence on frequency ω and local array vector \mathbf{s} , we have

$$\text{FT}\{WV\} = \sum_{\omega_1}^{\omega_2} \sum_n B_n \widehat{W}(\mathbf{k} - k_n \mathbf{d}). \quad (9)$$

The purpose of this exercise is to identify the optimal frequency range $\Delta\omega = \omega_2 - \omega_1$ over which to perform this operation.

Selection of the proper frequency band is critical to determining the most probable leak location and minimizing the number of required sensors. Three factors determine this frequency band: leak noise spectrum, array detector sensitivity, and noise transmission across structural features. A robust leak location system must operate in the intersection of these three criteria.

Basic turbulence theory [?] predicts the leak energy coupled into the plate will decrease with frequency, and in fact it is observed that no usable leak noise lies beyond roughly 400 kHz. This finding matches the sensitivity of the detector, which operates below 500 kHz.

Dicing the PZT array has previously been shown to improve leak location performance [?], but some residual transverse wave propagation in the crystal and overall reduced performance have still been observed from 75 to 275 kHz. Now that it is clear the integral stiffeners strongly influence guided wave transmission in the stiffened plate, we can rephrase the question concerning the optimal frequency and bandwidth for leak location. Replacing the PZT array, which must make mechanical contact to the plate, with a contactless optical probe completes the elimination of perturbing elements that would tend to obscure the best choice for the frequency and bandwidth.

Forty-three different simulated leak locations have been arbitrarily distributed across the surface of the plate. The direction of wave propagation is then determined from Eq. (??).

Two different candidate algorithms are considered. The first, termed *in situ* calibration, relies on simulated leaks with a known position. The optimal system consists of the set of frequency bands that correctly locate the known leak. The most straightforward implementation pairs a contact source transducer with each detector array. Location of one simulated leak at a time with each of the other sensors determines the calibration. The disadvantage of this method is that it requires additional complexity, power, and cost of additional source transducers. To achieve the simplest implementation, this method is not recommended. The second method, termed *wide-bandwidth* analysis, simply uses the full functional range of the array detector. By integrating over all available frequencies that may provide a correct answer, the frequency-dependent reflections tend to cancel destructively, while the correct signals reinforce.

The results of one of these tests for a 25-kHz frequency range are plotted in Fig. ?? . The spatial Fourier transform is zero-padded to 128×128 points in the x and y directions and uses a rectangular window. Each data point in the plot has been integrated with a 25-kHz bandwidth from 75 to 100 kHz. After summing, the data is integrated along a set of radial lines with 0.5° resolution. The angle with the largest integral is selected and plotted at each source point with a solid line. Each “x” in the figure corresponds to a simulated leak location, and the single circle shows the location on the 6×6 -foot plate of the scanned laser vibrometer array. The arrows at each “x” correspond to the most likely direction of the arriving wave vector, as measured at the open circle. The arrow lengths have been scaled for ease of interpretation so they nearly reach the detector. The diagonal dashed lines represent the low aspect-ratio integral stiffeners. Figure ?? shows the results of all 43 tests with the wavenumber map integrated over a frequency range extending from 75 to 100 kHz, as described in [?]. For each test, only the strongest observed wavenumber has been sampled and plotted. Although some of the simulated leaks are correctly located by the laser vibrometer array in Fig. ??, the performance is generally quite poor when the 75-100 kHz frequency range is used. Many of the arrows are not pointing even approximately toward the location of the array.

Contrast this behavior with the measurements of the same test analyzed in a frequency

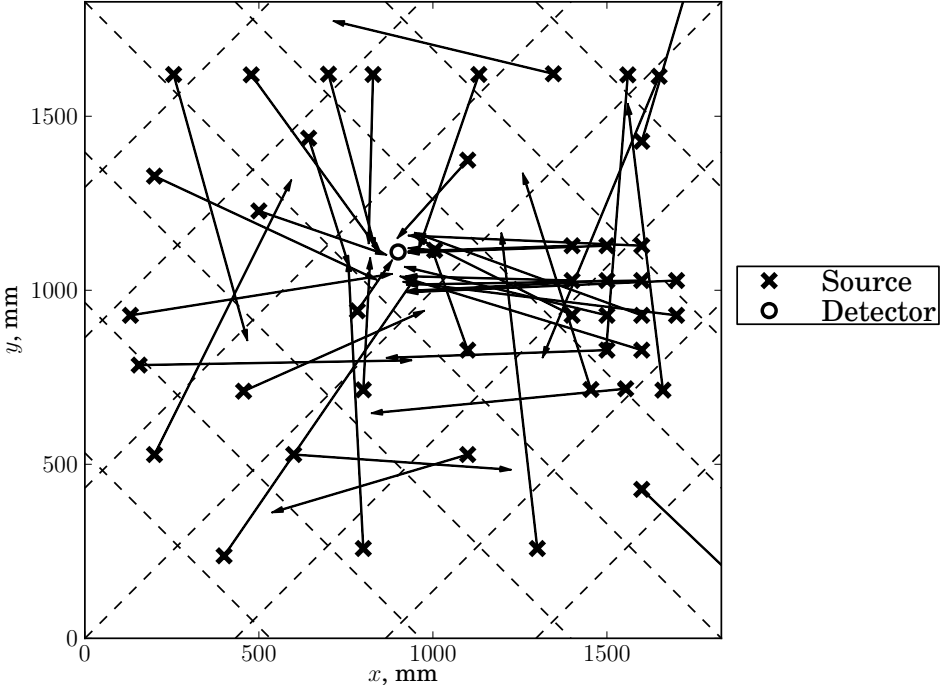


Figure 6: Leak location results for frequencies from 75-100 kHz. The “x” markings show simulated leak locations, and the circle near the plate center shows the detector array position. The diagonal dashed lines are the locations of the integral stiffeners.

range from 375–400 kHz, as shown in Fig. ???. In this figure, essentially none of the

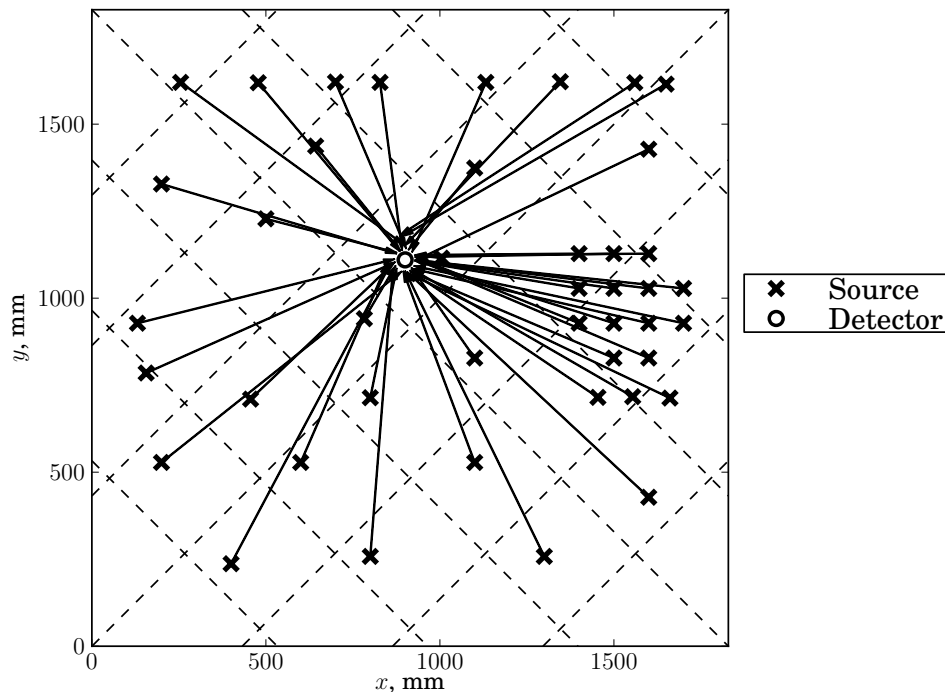


Figure 7: Leak location results for frequencies in the range 375–400 kHz. The “x” markings show simulated leak locations, and the circle shows the detector array position. The diagonal dashed lines are the integral stiffeners. The arrows, indicating the predicted source directions based on the measured data, are now essentially all correct.

prediction measurements, even across as many as four stiffeners, is in error by more than 5° for the range 375–400 kHz. Because there are no complicating coupling variations, such as when using the PZT array detector, the behavior observed here must be entirely the result of the acoustic response of the integrally stiffened plate.

These observations using the laser vibrometer detector match very closely the measured performance of the PZT array detector, when it is also operated in this frequency range. Furthermore, these results are completely consistent with the stiffener transmission coefficients in Fig. ??. In tests with either the laser vibrometer or PZT array, leak location occurs with consistent accuracy mainly above 275 kHz. Although the test data shown in Fig. ?? indicate clearly that the guided wavevectors are not always normal to the stiffener, as they are in the transmission coefficients plotted in Fig. ??, the data of

Fig. ?? strongly suggest that normal-incidence transmission still is a good indicator of leak location performance.

The strong correlation described above between stiffener transmission and accurate leak location seems to favor *in situ* calibration as the preferable algorithm for frequency range selection. Not all stiffener geometries, however, have such wide pass-bands and stop-bands. For the tall stiffener (2.54 mm wide by 22 mm high) Fig. ?? shows the measured and calculated transmission coefficients, but with much narrower pass and stop-bands. Extrapolating this behavior to the case of off-normal incidence guided waves across multiple stiffeners is likely more hazardous than for the short stiffeners.

In fact, no such extrapolation is necessary. Figure ?? shows the same data as those

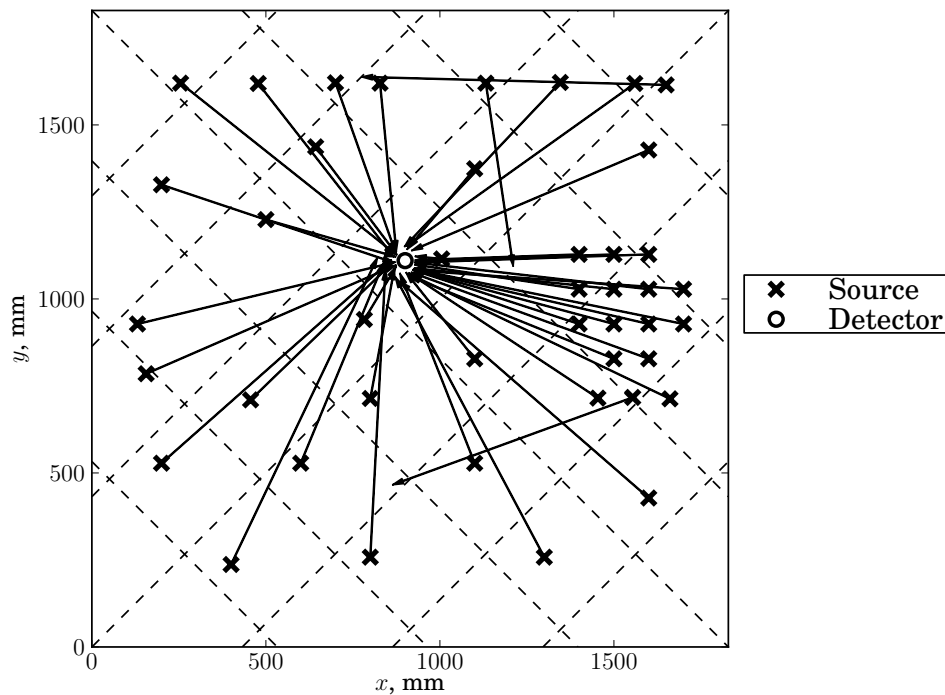


Figure 8: Normalized leak location maps for frequencies in the range 100–475 kHz. The “x” markings show simulated leak locations, and the circle shows the detector array position. The diagonal dashed lines are the integral stiffeners. The arrows, indicating the predicted source directions based on the measured data, are still nearly all correct, as they were in Fig. ??.

presented in Figs. ??–??, but with the maps normalized (L_1 norm of energy over 2-D maps

at each frequency) and integrated from 100 to 475 kHz. Normalization prevents a single spurious frequency from dominating the entire result. This *wide-bandwidth* algorithm demonstrates accurate leak location for 40 of the 43 tests. Although this result does not quite match the nearly perfect performance of Fig. ??, it does demonstrate that a simpler, more robust strategy can still locate leaks with high accuracy. A subtle unstated assumption here is that the acoustic array has a perfectly flat frequency response over the range of interest, which will not occur in any practical device. To compensate for that dependence, which can include coupling variations and wave damping, we would need to reformulate the protocol to give extra weight to those frequency ranges where the signal is stronger owing to these extrinsic effects.

4 SUMMARY AND CONCLUSIONS

Measurements and calculations have been performed of guided plate wave transmission and reflection at rectangular geometric obstructions, such as stiffeners, in an integrally stiffened isotropic plate. The results of the transmission measurements are in acceptably good agreement with first-principles BEM calculations and provide physical insight into the performance of the method of leak location which stimulated this study. As a by-product of this investigation we have demonstrated that a simple and robust frequency selection rule is represented by the inclusion of the entire reception bandwidth of the ultrasonic array sensor. Taken together with the known noise spectrum of the leak and the response of PZT array detector, these results provide the necessary guidance for frequency range selection.

Further investigations might include the examination of the angular dependence of guided wave transmission and mode conversion at off-normal incidence on an integrally stiffened plate. Although the transmission coefficients for guided plate waves at normal incidence on a stiffener are only part of the problem of stiffener scattering, this information does provide partial guidance for how to proceed with frequency selection in the leak location problem.

ACKNOWLEDGEMENT

This work is funded under NASA STTR #NNJ08JD11C through subcontract #2008-08-307 with Invocon, LLC.

References

- [1] D. S. F. Portree and J. P. Loftus, Jr, “Orbital debris: A chronology,” NASA Technical Paper *TP-1999-208856* (1999).
- [2] D. J. Kessler, “Sources of orbital debris and the projected environment for future spacecraft,” *J. Spacecraft* **18**, 357-360 (1981).
- [3] S. D. Holland, D. E. Chimenti, R. A. Roberts, and M. Strei, “Locating air leaks in manned spacecraft using structure-borne noise,” *J. Acoust. Soc. Am.* **121**, 3484–3492 (2007).
- [4] D. C. Gazis, “Three-Dimensional Investigation of the Propagation of Waves in Hollow Circular Cylinders. II. Numerical Results” in *J. Acoust. Soc. Am.* **31**(5), pp. 573-578, (1959).
- [5] D. Alleyne, P. Cawley, “A two-dimensional Fourier transform method for the measurement of propagating multimode signals” in *J. Acoust. Soc. Am.* **89**(3), pp. 1159-1168, (1991).
- [6] S. D. Holland, R. A. Roberts, D. E. Chimenti, and M. Strei, “Leak detection in spacecraft using structure-borne noise with distributed sensors,” *Appl. Phys. Lett.* **86**, 174105-1–3 (2005).
- [7] S. D. Holland, R. A. Roberts, D. E. Chimenti, Jun-Ho Song, “An ultrasonic array sensor for spacecraft leak direction finding,” *Ultrasonics* **45**, 121–126 (2006).

- [8] R. A. Roberts, “Guided wave propagation in integrally stiffened plates,” in *Review of Progress in Quantitative Nondestructive Evaluation*, vol. 27, D. O. Thompson, D. E. Chimenti, Eds. (AIP Press, New York, 2008), pp. 170–177.
- [9] B. Morvan, N. Wilie-Chancellier, H. Duflo, A. Tinel, J. Duclos, “Lamb wave reflection at the free edge of a plate” in *J. Acoust. Soc. Am.* **113**(3), pp. 1417-1425, (2003).
- [10] R. A. Roberts, “Plate wave transmission/reflection at geometric obstructions: model study,” in *Review of Progress in Quantitative Nondestructive Evaluation*, vol. 29, D. O. Thompson, D. E. Chimenti, Eds. (AIP Press, New York, 2010), pp. 192–199.
- [11] W. Sachse, Y.-H. Pao, “On the determination of phase and group velocities of dispersive waves in solids” in *J. Appl Phys.*, **49**(8), pp. 4320-4327, (1978).
- [12] J. D. Achenbach, *Reciprocity in Elastodynamics*, (Cambridge Univ Press, London, 2003).
- [13] S. B. Pope, *Turbulent Flows*, (Cambridge University Press, London, 2000).